Draft version December 16, 2016
Preprint typeset using LaTeX style AASTeX6 v. 1.0

arXiv:1612.05027v1 [astro-ph.GA] 15 Dec 2016

THE FORMATION OF SECONDARY STELLAR GENERATIONS IN MASSIVE YOUNG STAR CLUSTERS FROM RAPIDLY COOLING SHOCKED STELLAR WINDS

R. Wünsch, J. Palouš
Astronomical Institute, Academy of Sciences of the Czech Republic, Boční II 1401, 141 31 Prague, Czech Republic

G. Tenorio-Tagle
Instituto Nacional de Astrofísica Optica y Electrónica, AP 51, 72000 Puebla, México

S. Ehlerová
Astronomical Institute, Academy of Sciences of the Czech Republic, Boční II 1401, 141 31 Prague, Czech Republic

ABSTRACT

We study a model of *rapidly cooling shocked stellar winds* in young massive clusters and estimate the circumstances under which secondary star formation, out of the reinserted winds from a first stellar generation (1G), is possible. We have used two implementations of the model: a highly idealized computationally inexpensive spherically symmetric semi-analytic model, and a complex three-dimensional radiation-hydrodynamic simulations, and they are in a good mutual agreement. The results confirm our previous findings that in a cluster with 1G mass 10^7 M$_\odot$ and half-mass radius 2.38 pc, the shocked stellar winds become thermally unstable, collapse into dense gaseous structures that partially accumulate inside the cluster, self-shield against ionizing stellar radiation and form the second generation (2G) of stars. We have used the semi-analytic model to explore a subset of the parameter space covering a wide range of the observationally poorly constrained parameters: the heating efficiency, $\eta_{\rm he}$, and the mass loading, $\eta_{\rm ml}$. The results show that the fraction of the 1G stellar winds accumulating inside the cluster can be larger than 50% if $\eta_{\rm he} \lesssim 10\%$ which is suggested by the observations. Furthermore, for low $\eta_{\rm he}$, the model provides a self-consistent mechanism predicting 2G stars forming only in the central zones of the cluster. Finally, we have calculated the accumulated warm gas emission in the H30α recombination line, analyzed its velocity profile and estimated its intensity for super star clusters in interacting galaxies NGC4038/9 (Antennae) showing that the warm gas should be detectable with ALMA.

Keywords: HII regions — galaxies: globular clusters: general — star clusters: general — galaxies: ISM — galaxies: star formation

1. INTRODUCTION

Young massive clusters with masses $M_{\rm SC} = 10^5$ – 10^7 M$_\odot$ observed in nearby starburst galaxies (e.g. Portegies Zwart et al. 2010; Whitmore & Schweizer 1995; Gilbert & Graham 2007; Mengel et al. 2008; Melo et al. 2005; Westmoquette et al. 2007, and references therein) include high numbers of massive stars concentrated within a small volume (radius of a few parsecs). Winds of these stars collide with each other and convert their kinetic energy into heat resulting in a hot gas filling most of the cluster interior. The high thermal pressure of this gas drives a star cluster wind that becomes supersonic as it expands into the surrounding medium. Considering that global parameters of stellar winds vary on a time-scale which is longer than the wind crossing time through the cluster, Chevalier & Clegg (1985) found basic properties of the stationary (i.e. time independent) cluster wind by solving adiabatic, spherically symmetric hydrodynamic equations.

Silich et al. (2003) found that when radiative cooling of the hot shocked wind is taken into account, the stationary star cluster wind solution does not exist if the total cluster mechanical luminosity, $L_{\rm SC}$, exceeds the so called *critical luminosity*, $L_{\rm crit}$. The critical luminosity is a function of other cluster parameters, e.g. it can be shown that it is directly proportional to the star cluster radius $R_{\rm SC}$ (Silich et al. 2004). Since $L_{\rm SC}$ is directly proportional to the star cluster stellar mass, $M_{\rm SC}$, the condition for the existence of the stationary solution can be also formulated as an upper limit for the cluster compactness $C \equiv M_{\rm SC}/R_{\rm SC}$ (cnf. to Krause et al. 2016). Tenorio-Tagle et al. (2005b) hypothesized that in clusters with $L_{\rm SC} > L_{\rm crit}$, the mass reinserted by massive

stars (i.e. shocked stellar winds and supernova ejecta) accumulates in the cluster interior and feeds secondary star formation in situ. Tenorio-Tagle et al. (2007) confirmed the mass accumulation by 1D hydrodynamic simulations and found that such clusters present two qualitatively different regions (hence the solution was named *bimodal*) separated by the so called *stagnation radius*, $R_{\rm st}$: the mass inserted below it accumulates inside the cluster while the mass inserted above it leaves the cluster in a form of a cluster wind for which the stationary solution can be found. The process of mass accumulation in star clusters with a bimodal solution was explored by Wünsch et al. (2008) who ran 2D hydrodynamic simulations and found that parcels of the hot gas below the stagnation radius cool rapidly from $\sim 10^7$ K down to the minimum allowed temperature 10^4 K (motivated by the assumption that the gas is ionized by stellar radiation) and are subsequently compressed by the surrounding hot gas until they reach pressure equilibrium as dense warm clumps. The bimodal solution was further studied by Tenorio-Tagle et al. (2010) who estimated the shapes of recombination line profiles from 2D simulation, Silich et al. (2010) who applied it to high-redshift SCUBA galaxies with extremely high star formation rates, Hueyotl-Zahuantitla et al. (2010, 2013) who applied it to galactic nuclear star clusters, Wünsch et al. (2011) who calculated the time evolution of clusters evolving in the bimodal regime for the whole period of the existence of massive stars, and Tenorio-Tagle et al. (2013) who included cooling due to dust produced by supernovae.

This work follows up on two of our previous papers. In Palouš et al. (2013) we studied the properties of star cluster winds produced by sources representing first generation (1G) stars, distributed spatially according to a generalized Schuster function (Lohmann 1964; Ninkovic 1998). This is a more realistic stellar density profile of a cluster than the top-hat function (or even distribution of sources) used in previous works. In Palouš et al. (2014) we estimated the conditions under which the accumulated warm gas self-shields against the ionizing stellar EUV radiation (with photon energies above 13.6 eV) and cools below 10^4 K to form a second generation (2G) of stars. Here we model stellar clusters with a first generation of stars represented by a smooth distribution of mass and energy sources which follow the Schuster profile. We include radiative cooling of the gas, ionizing radiation of massive stars, and the gravitational field from the first stellar generation. We combine 3D radiation-hydrodynamic simulations (to calculate three models with high accuracy) and 1D semi-analytic models (to explore a larger parameter space). The simulations include an approximate model of star formation implemented through sink particles, the gas self-gravity, and gravity from sink particles. We concentrate on the first 3.5 Myr of the cluster evolution, i.e. before supernovae start to explode. This is due to our smooth insertion of mass and energy which cannot represent well discrete events such as SN explosions. (Note however that most groups have inserted SNe in this way, assuming a time averaged energy and mass input as inferred from the Starburst99 synthesis code (Leitherer et al. 1999)). Furthermore, the SN ejecta may be enriched by a non-negligible amount of dust, which is an agent capable of enhancing the cooling of the hot gas (Tenorio-Tagle et al. 2013) and this is not yet implemented in our model. The cluster evolution during the SN period will be described in a forthcoming paper (Jeřábková, in prep.).

Motivated by the observations, we introduced two additional parameters: the *heating efficiency* $\eta_{\rm he}$ and the *mass loading* $\eta_{\rm ml}$. The first one indicates the fraction of the mechanical energy of stellar winds that is transformed into thermal energy of the hot shocked gas inside the cluster. This may help to solve the discrepancy between the observed and the predicted X-ray luminosity of HII regions associated with young massive clusters (see e.g. Rosen et al. 2014, and the references therein). Silich et al. (2010) determined the heating efficiency of 10 young massive clusters in M82 galaxy from their corresponding HII regions radii and found $\eta_{\rm he} \lesssim 10\%$. Widths of recombination lines associated with super star clusters in the Antennae galaxies observed by Gilbert & Graham (2007) also suggest that $\eta_{\rm he} \lesssim 10\%$. Tenorio-Tagle et al. (2016) argue that the heating efficiency is effectively low if majority of massive stars end up as interacting binaries resulting in much lower stellar wind velocities. On the other hand, Strickland & Heckman (2009) estimated the total energy of winds of young massive clusters in M82 and found rather high values of $\eta_{\rm he} = 30 - 100\%$. The second parameter, mass loading $\eta_{\rm ml}$, describes an additional influx of primordial gas into the hot thermalized winds representing processes as for instance evaporation of dense pre-existing clouds inside the cluster or evaporation of envelopes and disks of young low-mass protostars and stars. A similar parameter was introduced in Silich et al. (2010). Mass loading is normalized by the mass insertion rate due to stellar winds, $\dot{M}_{\rm SC}$. Both parameters ($\eta_{\rm he}$ and $\eta_{\rm ml}$) are not particularly well constrained. Therefore, we let them vary in a wide range of values and explore the parameter space to understand how our results depend on them.

Our model predicts the formation of secondary stellar generations within the cluster, with the matter injected by the winds from massive stars of the first generation. This may be related to the multiple stellar populations found in globular clusters (see e.g. Bedin et al. 2004; Piotto et al. 2007; Bastian 2016, and references therein), and recently also in intermediate age massive clusters (e.g. Milone et al. 2009). Additionally, spectroscopic

observations revealed anti-correlations between certain pairs of light elements (e.g. sodium and oxygen; see Carretta et al. 2006, 2009) suggesting that a fraction of stars in globular clusters could form out of gas enriched by products of high-temperature H-burning, as those produced either in massive stars (Decressin et al. 2007a) or in Asymptotic Giant Branch stars (D'Ercole et al. 2010). Our model is not directly applicable to the formation of globular cluster, because we set the metallicity of the first generation stars to be solar for the sake of comparability with our previous works on super star clusters. However, the qualitative predictions of mass accumulation and secondary star formation are significant and robust. Furthermore, the rapidly cooling winds model presents multiple features that may help to eliminate some of the problems encountered by other self-enrichment scenarios. Specifically, it provides a mechanism to capture fast ($\gtrsim 1000\,\mathrm{km\,s^{-1}}$) stellar winds inside the cluster and it self-consistently predicts that under certain conditions, secondary star formation occurs in the very center of clusters. On the other hand, no completely satisfactory explanation of the multiple populations found recently in globular clusters exists, and this model would also suffer by similar problems as other scenarios based on self-enrichment by massive stars (see Bastian 2015, and references therein).

The paper is organized as follows: in §2 we describe the adopted physical model of the cluster, §3 and §4 introduce the semi-analytic and numerical codes used to calculate the model, respectively. Our results are presented in §5. Specifically, we give semi-analytic estimates of the mass necessary for self-shielding (§5.1), describe the radiation-hydrodynamic simulations confirming the estimates and calculate the synthetic emission line spectra of the simulated clusters (§5.2), use the semi-analytic estimates to explore a larger parameter space and predict certain properties of secondary stellar generations (§5.4). The implications of the results for the evolution of massive star clusters is discussed in §6, and our conclusions are formulated in §7.

2. PHYSICAL MODEL

We consider a young cluster with a first stellar generation (1G) of mass $M_{\rm SC} = 10^7\,\mathrm{M_\odot}$ formed abruptly at time $t = 0$. The stellar density $\rho_\star$ is given by the spherically symmetric Schuster distribution in a form

$$\rho_\star = M_{\rm SC} f_{\rm Sch}(r, \beta, R_c, R_{\rm SC}) \tag{1}$$

$$f_{\rm Sch}(r, \beta, R_c, R_{\rm SC}) = \begin{cases} \frac{C_{\rm Sch}}{[1+(r/R_c)^2]^\beta} & \text{for } r \le R_{\rm SC} \\ 0 & \text{for } r > R_{\rm SC} \end{cases} \tag{2}$$

$$C_{\rm Sch} = \frac{3}{4\pi} R_{\rm SC}^{-3} \left[{}_2F_1(\frac{3}{2}, \beta, \frac{5}{2}, -\frac{R_{\rm SC}^2}{R_c^2}) \right]^{-1} \tag{3}$$

where ${}_2F_1$ is the Gauss hypergeometric function, ${}_2F_1(3/2, \beta, 5/2, -(r/R_c)^2)$ hereafter abbreviated as $F_\beta(r)$, and $C_{\rm Sch}$ is the normalization constant. It has been shown by Ninkovic (1998) that the Schuster distribution with the slope $\beta = 1.5$ (see Equation 2) approximates well the King stellar surface density profile (King 1962). The King profile was originaly obtained for the globular clusters, however, it is also in a good agreement with the observed stellar surface density profiles of young massive clusters (e.g. Espinoza et al. 2009). Therefore, we use $\beta = 1.5$ for the all presented models. Values of the core radius, $R_c = 1.58\,\mathrm{pc}$, and the cluster radius, $R_{\rm SC} = 4.5\,\mathrm{pc}$, result in the half mass radius $R_h = 2.38\,\mathrm{pc}$ which is the same as for the uniform sphere with radius 3 pc. The corresponding gravitational potential $\Psi_\star$ can be obtained using a standard formula for the potential of the spherically symmetric density distribution (see e.g. Binney & Tremaine 2008)

$$\Psi_\star(r) = -GM_{\rm SC} \left\{ r^2 F_\beta(r) + \frac{3R_c^{2\beta}}{2(\beta-1)} \left[(R_c^2 + R_{\rm SC}^2)^{1-\beta} - (R_c^2 + r^2)^{1-\beta} \right] \right\} \tag{4}$$

where G is the gravitational constant. The escape velocity from radius r to infinity is $v_{\rm esc}(r) = \sqrt{|2\Psi_\star(r)|}$, and the free fall time from radius r to the center is

$$t_{\rm ff}(r) = \int_0^r \left(2[\Psi_\star(r) - \Psi_\star(r')]\right)^{-1/2} dr' \,. \tag{5}$$

Massive stars insert mass and mechanical energy into the cluster volume through their radiation driven winds. Following Chevalier & Clegg (1985) we assume that mutual collisions of individual stellar winds result in a hot gas filling most of the cluster volume (as validated numerically by Cantó et al. 2000 and others). We model this process by inserting mass and thermal energy smoothly into the cluster with total rates $\dot{M}_{\rm SC}$ and $L_{\rm SC}$, respectively. We assume that the sources follow the stellar distribution $\rho_\star$ and hence the mass and energy insertion rate densities are, respectively

$$q_m(r) = (1 + \eta_{\rm ml}) \dot{M}_{\rm SC} f_{\rm Sch}(r, \beta, R_c, R_{\rm SC}) \,, \tag{6}$$

$$q_e(r) = \eta_{\rm he} L_{\rm SC} f_{\rm Sch}(r, \beta, R_c, R_{\rm SC}) \,. \tag{7}$$

Here we use two additional parameters described in §1: the heating efficiency $\eta_{\rm he}$, which defines the fraction of the mechanical energy of individual stellar winds that is converted into the cluster wind thermal energy, and the mass loading $\eta_{\rm ml}$, which specifies the amount of additional material complementing the reinserted wind. In §5.1 and §5.2, we study in detail three models with $\eta_{\rm ml} = 1$ and $\eta_{\rm he} = 0.05$, 0.1 and 0.3 (see Table 1). Furthermore, we discuss the most important features of the model for a large range of these parameters $\eta_{\rm he} \in (0, 1)$, $\eta_{\rm ml} \in (0, 5)$ in §5.4.

Table 1. Parameters of all discussed models.

parameter	value	description
$M_{\rm SC}$	$10^7\,{\rm M}_\odot$	mass of the first stellar generation (1G)
β	1.5	slope of the 1G stellar density distribution
R_c	1.578 pc	core radius of the 1G radial distribution
$R_{\rm SC}$	4.5 pc	cluster radius, cutoff of the 1G radial distribution
$R_{\rm TH}$[a]	3.0 pc	radius of the cluster with top-hat 1G radial distribution
Z_0	0.02	metallicity of 1G stars
$\mu_{\rm i}$	0.609	mean mol. weight of hot and warm gas, $T \geq 10^4\,{\rm K}$
$\mu_{\rm c}$	2.35	mean mol. weight of cold gas, $T < 10^4\,{\rm K}$
$\mu_{\rm H}$[b]	1.273	mean mol. weight per hydrogen nuclei
$\eta_{\rm he}$[c]	$0.001 - 1$	heating efficiency
$\eta_{\rm ml}$[d]	$0 - 5$	mass loading

[a] $R_{\rm TH}$ is chosen so that the half-mass radius is the same as in the case of cluster with Schuster 1G distribution with parameters R_c and $R_{\rm SC}$ given above.

[b] Used for calculating n_i and n_e in cooling rate Q and recombination rate $\dot{N}_{\rm r}$.

[c] $\eta_{\rm he} = 0.05$, 0.1 and 0.3 for models A, B and C, respectively.

[d] $\eta_{\rm ml} = 1$ for models A, B and C.

The total amounts of mass and energy inserted into the cluster per unit time, $\dot{M}_{\rm SC}$ and $L_{\rm SC}$, respectively, are functions of time. They are determined using the stellar population synthesis code Starburst99 (Leitherer et al. 1999) by the procedure described in detail in Wünsch et al. (2011). It is assumed that 1G stars were formed instantaneously with the standard Kroupa initial mass function (Kroupa 2001); the Geneva stellar evolution tracks with the high mass loss wind model are used (see Leitherer et al. 1992, for details). The metallicity of the gas, Z, is also time-dependent however, at any given time, we assume that it presents a uniform value within the whole computational domain. This is given by equation:

$$Z(t) = \frac{\dot{M}_{\rm metals} + \eta_{\rm ml} Z_0 \dot{M}_{\rm SC}}{(1+\eta_{\rm ml})\dot{M}_{\rm SC}} \qquad (8)$$

where $Z_0 = Z_\odot$ is the metallicity of the first stellar generation and $\dot{M}_{\rm metals}$ is the total amount of elements heavier than He inserted by massive stars per unit time as provided by Starburst99. Note that it is always $\dot{M}_{\rm metals} \geq Z_0 \dot{M}_{\rm SC}$ (metallicity of stellar winds is at least the metallicity of the gas from which the stars were formed), and therefore $Z(t) \geq Z_0$ all the time.

The gas inserted into the cluster by 1G stars rapidly establishes a star cluster wind. This process is described by the hydrodynamic equations including terms for energy losses due to radiative cooling and eventually for gravity (of stars and self-gravity of the gas). These equations are accompanied by the ideal gas equation of state in a form

$$P = \frac{\rho k_{\rm B} T}{\mu m_{\rm H}}\,, \qquad (9)$$

where P, ρ and T are gas pressure, density and temperature, respectively; $k_{\rm B}$ is the Boltzmann constant and $m_{\rm H}$ is the hydrogen nuclei mass. The mean molecular weight μ is either $\mu = \mu_i = 0.609$ for the hot and warm gas with $T \geq 10^4\,{\rm K}$ (assuming it is ionized) or $\mu = \mu_c = 2.35$ for smaller temperatures (assuming it is molecular). We do not consider μ of the atomic phase, because the semi-analytic model describes only the hot ionized gas, and because the mass of the atomic phase is negligible in numerical models as the gas densities are so high that the gas shielded[1] against ionizing radiation cools down to $\sim 10\,{\rm K}$ almost immediately. We define also the mean molecular weight per hydrogen nuclei $\mu_{\rm H} = 1.273$ and use it to calculate electron and ion particle densities needed for radiative cooling computations: $n_e = n_i = \rho/\mu_{\rm H}$.

The exact form of the hydrodynamic equations for the semi-analytic model differs from those obtained for the numerical model, because the former ones are 1D spherically symmetric and time independent, while the latter ones are 3D time dependent and include more physical effects as for instance self-gravity and EUV radiation. Both sets of equations are explicitly given in sections §3 and §4, respectively. All discussed parameters of the model are summarized in Table 1.

3. SEMI-ANALYTIC CODE

We use the semi-analytic code developed by Silich et al. (2004) to estimate the amount of mass accumulated inside the cluster. This code searches for the stationary solution for the hot star cluster wind and in case it does not exist, it calculates how much mass has to be removed

[1] We use the words "shielded", "shielding" and "self-shielding" in the following way: the gas is called shielded when all ionizing radiation has been absorbed before reaching it; the gas is called shielding when it is absorbing the radiation that keeps it warm and ionized. We call the whole object (usually clump or stream) self-shielding when it consists of both shielding and shielded gas.

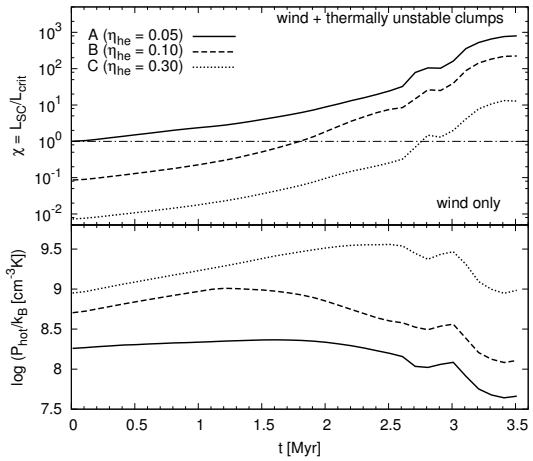

Figure 1. Top: evolution of the ratio of the cluster mechanical luminosity to the critical luminosity, $\chi \equiv L_{\rm SC}/L_{\rm crit}$, for the models A (solid), B (dashed) and C (dotted) with parameters given in Table 1. The dash-dotted line is the $\chi = 1$ line separating regions with the quasi-adiabatic behavior (below) and the rapidly cooling winds (above). Bottom: evolution of the mean pressure of the hot gas below $R_{\rm SC}$ approximated by the pressure at the stagnation radius calculated by the semi-analytic code for a cluster with top-hat stellar density profile and $R_{\rm TH} = 3\,$pc.

from the hot phase to allow the stationary solution existence. It is computationally much cheaper than full radiation-hydrodynamic simulations and therefore it allows us to explore the parameter space in §5.4. The procedure to use the code for considering an evolving cluster is described by Wünsch et al. (2011) and we briefly summarize it here for the convenience of the reader. The implementation of the semi-analytic code allows only sources with a top-hat radial density profiles, i.e. the mass and energy deposition rate densities, q_m and q_e, are spatially constant within the cluster. Therefore, clusters with the Schuster density profile used in this work are approximated by top-hat density profiles with the same half-mass radius $R_h = 2.38\,$pc resulting in the top-hat cluster radius $R_{\rm TH} = 3\,$pc. The gravity acting on the hot gas is neglected, since the thermal energy of the hot gas is always higher than its potential energy in the gravitational field of the cluster. However, the gravity is taken into account in estimates of the fraction of the reinserted mass that stays in the cluster (see Equations (13) and (14) below).

We assume that mass and energy deposition rate densities, q_m and q_e, vary on a substantially longer time-scale than the cluster wind crossing time. Then, for a cluster at a given time, we can search for a stationary wind solution by solving the spherically symmetric hydrodynamic equations:

$$\frac{1}{r^2}\frac{d}{dr}(\rho u r^2) = q_m \tag{10}$$

$$\rho u \frac{du}{dr} = -\frac{dP}{dr} - q_m u \tag{11}$$

$$\frac{1}{r^2}\frac{d}{dr}\left[\rho u r^2 \left(\frac{u^2}{2} + \frac{\gamma}{\gamma-1}\frac{P}{\rho}\right)\right] = q_e - Q \tag{12}$$

where ρ, u and P are the wind density, velocity and pressure, respectively. The energy equation (12) includes the cooling term $Q = n_i n_e \Lambda(T, Z)$ where $n_i = n_e = \rho/\mu_{\rm H}$ are the ion and electron number densities, Z is the gas metallicity given by Eq. 8 and $\Lambda(T, Z)$ is a cooling function calculated by Schure et al. (2009). The pressure is calculated using the ideal gas equation of state (9) with $\mu_i = 0.609$.

As shown by Tenorio-Tagle et al. (2007), Equations (10) – (12) have a solution for all radii only if the cluster mechanical luminosity, $L_{\rm SC}$, does not exceed a certain critical value, $L_{\rm crit}$. This critical luminosity can be found using a bisection method by varying $L_{\rm SC}$ and checking whether the solution of (10) – (12) exists or not. In order to obtain a more accurate value of $L_{\rm crit}$ for clusters with a Schuster density profiles, we corrected $L_{\rm crit}$ by a constant factor 3.5 found by comparison with 1D numerical simulations by Palouš et al. (2013) (see their Figure 6). We define a ratio between the cluster mechanical luminosity and its critical value, $\chi = L_{\rm SC}/L_{\rm crit}$, and plot its time evolution for models A, B and C in Figure 1 (top panel).

If $\chi > 1$, the stationary solution of Equations (10) – (12) does not exists for the whole cluster volume. However, it is still possible to find a solution in the region $r > R_{\rm st}$ where $R_{\rm st}$ is the so called stagnation radius below which the wind velocity is zero. In Wünsch et al. (2011) we assumed that all gas inserted below $R_{\rm st}$ accumulates inside the cluster. Here we find through hydrodynamic simulations (see §5.2 below) that models with a negative stellar radial density gradient (e.g. Schuster profiles) behave differently. The wind velocity is positive in the whole cluster volume and no stagnation radius exists even for $\chi > 1$. In our calculations, dense clumps are still formed through thermal instabilities inside the cluster. As they have positive radial velocities "inherited" from the wind gas from which they form, in the absence of gravity, they would leave the cluster. However, if gravity is taken into account, clumps formed at smaller radii, with radial velocities smaller than the escape velocity (see below), are captured and fall into the cluster center.

The fraction of the inserted gas that ends up in dense clumps can be estimated by comparing the mass deposition rate density of a given model q_m with the cor-

responding quantity $q_{m,\rm crit}$ of the model with the same parameters but a mechanical luminosity $L_{\rm SC}$ equal to $L_{\rm crit}$. This is because clump formation effectively lowers the density of the hot medium down to the level obtained when $\chi = 1$. The clumps acquire positive radial velocities similar to that of the wind at the radius where they form. Thus we define the escape radius $R_{\rm esc}$ as the distance from the cluster center where the wind velocity u equals the cluster escape velocity:

$$u(R_{\rm esc}) = v_{\rm esc}(R_{\rm esc}) \equiv \sqrt{|2\Psi_\star(R_{\rm esc})|} \qquad (13)$$

where $\Psi_\star$ is given by Equation (4). Then, we assume that all the clumps that form below $R_{\rm esc}$ are captured and clumps that form above $R_{\rm esc}$ leave the cluster with the wind. Therefore, the amount of gas accumulated up to a certain time t is estimated as

$$M_{\rm acc}(t) = \int_{t_{bs}}^{t}\int_{0}^{R_{\rm esc}} [q_m(r,t') - q_{m,crit}(r,t')]drdt' \qquad (14)$$

where $t_{\rm bs}$ is the time at which χ exceeds 1 and thermal instabilities start to appear inside the cluster. Note that in this approach, the accumulated mass, $M_{\rm acc}$, is overestimated as it ignores the hydrodynamic forces from the wind pushing the clumps outwards. On the other hand, $M_{\rm acc}$ is underestimated as Equation (14) ignores the gravitational force caused by the accumulated gas and the forming secondary stellar generation. However, a comparison for models A, B and C, between $M_{\rm acc}$ and $M_{\rm acc}^{\rm num}$ obtained from numerical simulations that include both the above effects, suggests that the errors are not large (see Table 2 and Figure 7).

4. NUMERICAL CODE

The numerical model is based on the three-dimensional, adaptive mesh refinement (AMR) code FLASH v4.2.1 (Fryxell et al. 2000). The AMR is handled by the PARAMESH library (MacNeice et al. 2000), the whole code is parallelized via domain decomposition under the Message Passing Interface (MPI). The hydrodynamic equations are solved using a modified version of the Piecewise Parabolic Method (PPM Colella & Woodward 1984) with the time-step controlled by the Courant-Friedrichs-Lewy criterion. They have a form

$$\frac{\partial\rho}{\partial t} + \nabla\cdot\rho\mathbf{u} = q_m \qquad (15)$$

$$\frac{\partial\rho\mathbf{u}}{\partial t} + \nabla\cdot\rho\mathbf{u}\mathbf{u} + \nabla P = \rho\nabla\Psi - q_m\mathbf{u} \qquad (16)$$

$$\frac{\partial\rho E}{\partial t} + \nabla\cdot(\rho E + P)\mathbf{u} = \rho\mathbf{u}\cdot\mathbf{g} + q_e - Q \qquad (17)$$

where ρ, $\mathbf{u}$ and P are the gas density, velocity and pressure, respectively, and $E = P/[(\gamma-1)\rho] + u^2/2$ is the total energy per unit mass with γ being the ratio of specific heats. The mass and energy deposition rate q_m and q_e are given by Equations (6) and 7, respectively, and their time evolution is obtained from Starburst99 code as described in §3. The cooling term Q is calculated using a procedure based on sub-cycling described in Wünsch et al. (2008). The gravitational potential Ψ consists of three parts, $\Psi = \Psi_\star + \Psi_{\rm s} + \Psi_{\rm g}$, where $\Psi_\star$ is the potential of 1G stars given by Equation (4), $\Psi_{\rm s}$ is the potential of sink particles (see below) calculated by direct force summation, and $\Psi_{\rm g}$ is the potential of the gas obtained by solving the Poisson equation

$$\nabla^2\Psi_{\rm g} = 4\pi G\rho\ . \qquad (18)$$

Equation (18) is solved using the tree code algorithm described in Wünsch et al. (2017, in prep.), it also provides the gravitational acceleration g corresponding to Ψ. The set of Equations (15)–(17) is closed by the equation of state as in (9) with mean molecular weights μ_i and μ_c for the appropriate temperature regimes (see Table 1).

The ionizing radiation of stars is included using module OpticalDepth of the radiation transport code TreeRay described in Wünsch et al. (2016, in prep.). Instead of calculating the radiation transport exactly, it assumes that the whole computational domain is embedded in a bath of ionizing radiation with a uniform photon flux coming from all directions. The photon flux is approximated by flux $F_{\rm UV}$ in the center of a sphere with radius $R_{\rm TH}$ and uniform distribution of radiation sources with the total photon production rate $\dot{N}_{\rm UV}$ given by the Starburst99 code for clusters with the selected parameters (see also Equation (19) in Palouš et al. 2014)

$$F_{\rm UV} = (3\dot{N}_{\rm UV})/(16\pi R_{\rm TH}^3)\ . \qquad (19)$$

Using the generalized algorithm TreeCol developed by Clark et al. (2012), the OpticalDepth module calculates the emission measure EM_j for each grid cell and for each direction

$$EM_j = \int_0^\infty \left(\frac{\rho(s,j)}{\mu_{\rm H}}\right)^2 ds \qquad (20)$$

where index j runs over 12 directions, the minimum number defined by the HealPix library (Górski et al. 2005) and $\rho(s,j)$ is the gas density in direction j at distance s from the cell. Invoking the on-the-spot approximation (Osterbrock 1974) and assuming that EUV photons are destroyed along the incoming ray by recombinations to other than the fundamental level, the number of ionizing photons $n_{\rm UV}$ entering the grid cell is

$$n_{\rm UV} = \sum_{j=1}^{12} A_{\rm surf,j} H(F_{\rm UV} - EM_j/\alpha_{\rm B}) \qquad (21)$$

where $A_{\rm surf,j} = [(\pi/48)^{(1/2)}{\rm d}V]^{(2/3)}$ is a fraction of the grid cell surface associated with direction j with ${\rm d}V$ being the grid cell volume, $\alpha_{\rm B} = 2.7\times10^{-13}\,{\rm cm^3 s^{-1}}$ is the recombination coefficient into excited states only and H

is the Heaviside step function. Subsequently, the grid cell is assumed to be ionized and its temperature is maintained at $T_i = 10^4\,\mathrm{K}$ if $n_{\mathrm{UV}} > 0$. Otherwise, if $n_{\mathrm{UV}} = 0$, the grid cell is allowed to cool to lower temperatures (which in the majority of cases means that it quickly cools down to the minimum allowed temperature 10 K because of its high density).

As the cold gas evolves under the influence of its own gravity it may become gravitationally unstable and collapse if its mass exceeds the Jeans mass. Therefore we include the sink particles module of FLASH (Federrath et al. 2010). If the gas density in a certain grid cell exceeds a threshold ρ_{sink} and if the gas within the so called accretion radius, r_{acc}, fulfills a number of criteria, a sink particle is created. The criteria are: (i) the cell is at the highest refinement level, (ii) the cell represents a local minimum of Ψ_g, (iii) the mass exceeds the Jeans mass, (iv) the flow is converging ($\nabla \cdot \mathbf{u} < 0$), (v) the gas is gravitationally bound, and (vi) the region does not overlap with some other sink particle. Additionally, a fraction of gas with density exceeding ρ_{sink} within r_{acc} of each particle is accreted onto it, i.e. the gas density is truncated to ρ_{sink} and the mass is added to the mass of the sink particle. For all models presented here we set $\rho_{\mathrm{sink}} = 10^{-17}\,\mathrm{g\,cm^{-3}}$ and $r_{\mathrm{acc}} = 0.05\,\mathrm{pc}$ corresponding to 2.5× grid cell size, as recommended by authors of the sink particles module of the code. With these values, it is not possible to follow the fragmentation process down to the mass of individual stars. Therefore, sink particles here represent "clusters" or "associations" of secondary stellar generations rather than individual stars. The number of sink particles depends on the simulation resolution, however, the total mass in sink particles does not. We checked this by comparing runs A, B and C with their low-resolution counterparts calculated for the whole time at 128^3 grid.

We simulate models A, B and C for their first 3.5 Myr of evolution, *i.e.* before SNe start to explode. The computational domain has size $(10\,\mathrm{pc})^3$ and all outer boundary conditions are set to outflow. Most of the time is computed on a uniform 128^3 grid, however, several selected periods are calculated with AMR at the maximum resolution corresponding to 512^3.

4.1. *Synthetic spectra*

We calculate the synthetic spectra of a hydrogen recombination line formed in the warm gas (mainly in thermally unstable clumps) present in the simulations. This will allow to compare the calculated models with radio observations (e.g. in mm-wavelengths by ALMA). We choose the H30α with rest frequency $\nu_0 = 231.9\,\mathrm{GHz}$ due to its proximity to the frequency of molecular CO(2-1) line allowing eventually to probe both ionized and molecular gas with a single observation. We assume that the emission is optically thin and verify that such is the case afterwards by calculating the maximum optical depth in the simulations. This allows us to treat each grid cell separately and calculate its line emission $T_{\mathrm{L,cell}}$ as (Rohlfs & Wilson 2004)

$$T_{\mathrm{L,cell}} = 1.92 \times 10^3 \left(\frac{T_e}{K}\right)^{-3/2} \left(\frac{EM_{\mathrm{cell}}}{\mathrm{cm^{-6}pc}}\right) \left(\frac{\Delta\nu}{\mathrm{kHz}}\right)^{-1} \tag{22}$$

where $EM_{\mathrm{cell}} = (\rho/\mu_{\mathrm{H}}/m_{\mathrm{H}})^2 \mathrm{d}s$ is the emission measure of the cell, T_e is the electron temperature assumed to be the same as the gas temperature T in the grid cell, $\mathrm{d}s$ is the linear cell size and $\Delta\nu = \Delta v \nu_0/c$ is the width of a frequency bin corresponding to the velocity bin width Δv. In all calculations presented here we cover the velocity range $(-400, 400)\,\mathrm{km\,s^{-1}}$ with 500 bins leading to $\Delta v = 1.6\,\mathrm{km\,s^{-1}}$ and $\Delta\nu = 1240\,\mathrm{kHz}$.

For a given line-of-sight aligned with one of the Cartesian axes, we calculate the line profile T_{L} by summing up all contributions $T_{\mathrm{L,cell}}\mathrm{d}s$ intersecting with the line-of-sight and distributing them into velocity bins according to the velocity of the grid cell convolved with the Gaussian of width $\sigma = k_{\mathrm{B}}T/(\mu_e m_{\mathrm{H}})$ to account for thermal broadening. We present position-velocity diagrams of our simulations at $z = 0$ plane integrated along the y-direction in Figure 6. Additionally, we sum up contributions of all lines-of-sight $T_{\mathrm{L}}(\mathrm{d}s)^2$ and normalize the result by $\pi D_{\mathrm{res}}^2/4$ in order to obtain the brightness temperature profile T_b as seen by a telescope with angular resolution D_{res}.

Finally, we calculate the maximum optical depth by summing up individual grid cell contributions

$$\tau_{\mathrm{L,cell}} = 1.92 \times 10^3 \left(\frac{T_e}{K}\right)^{-5/2} \left(\frac{EM_{\mathrm{cell}}}{\mathrm{cm^{-6}pc}}\right) \left(\frac{\Delta\nu}{\mathrm{kHz}}\right)^{-1} \tag{23}$$

along each line-of-sight for each frame of each simulation. We found that the integrated value τ_{L} never exceeds 10^{-2} justifying the assumption of an optically thin approximation.

5. RESULTS

5.1. *Estimate of the shielding mass*

The evolution of a growing dense clump immersed in the radiation field of the cluster was discussed in Palouš et al. (2014). It was shown there that the clump mass M_{c} becomes larger than the shielding mass $M_{\mathrm{c,sh}}$, rather early in the cluster evolution. $M_{\mathrm{c,sh}}$ is the mass of the clump needed to self-shield its interior against the ionizing radiation. We concluded that clumps may become quickly seeds of secondary stellar generations formed out of stellar wind matter carrying the hydrogen burning products originating in the stellar interiors.

By analyzing simulations of models A, B and C we

found that self-shielding of the dense gas typically appears in two qualitatively different configurations. One possibility is that the warm dense gas falls into the cluster center, accumulates there and only when its mass exceeds a certain value, it begins to shield itself against the EUV radiation, allowing its central regions to cool down and collapses into sink particles. We call this configuration *self-shielding of the central clump*. Another possibility is that the warm dense gas infalling towards the center along radial streams becomes self-shielding even before reaching the center. We call this configuration *self-shielding of infalling streams*. The difference between the two scenarios is astrophysically interesting, because in the former case, the second stellar generation is formed only in the very center of the cluster, while in the latter one, the stars of the second generation are formed everywhere in the 1G cluster volume.

Before we derive an equation for the shielding masses in the two previously described possibilities, we consider a simple configuration-independent threshold, $M_{\rm max,sh}$ for the maximum mass before the self-shielding occurs, based on the number of available EUV photons from all stars in the cluster. A more massive object or a group of objects, must include self-shielding regions regardless the geometry, as there are not sufficient EUV photons to keep them fully ionized. Therefore, in the calculations, we assume that a central clump or an infalling stream becomes self-shielding whenever its mass exceeds $M_{\rm max,sh}$, even in cases when its mass is below geometry dependent criteria $M_{\rm c,sh}$ or $M_{\rm s,sh}$ (see below)[2]. Assuming that the warm gas is in pressure equilibrium with the hot gas, one can calculate the warm gas mass, $M_{\rm max,sh}$, whose total recombination rate is equal to the total photon production rate of the cluster $\dot{N}_{\rm UV}$:

$$M_{\rm max,sh} = \frac{\mu_i m_H}{\alpha_{\rm B}} \frac{kT_4}{P_{\rm hot}} \dot{N}_{UV} \ . \qquad (24)$$

where $T_4 = 10^4\,{\rm K}$ is the temperature of the warm ionized gas, and $P_{\rm hot}$ is the pressure of the hot gas that can be approximated by the pressure at the stagnation radius calculated by the semi-analytic code. Since $P_{\rm hot}$ regulates the volume and therefore the density of the warm gas and through it the total number of recombinations, it is then the quantity that mainly determines the shielding mass in any configuration. Figure 1 (bottom panel) shows the time evolution of $P_{\rm hot}$.

5.1.1. *Self-shielding of the central clump*

We assume that the mass of the central clump, $M_{\rm c}$, is the same as the total amount of the accumulated gas, $M_{\rm acc}$, given by Equation (14). Pressure equilibrium between the central clump and hot gas yields the clump radius

$$R_c = \frac{3}{4\pi} M_{\rm c}^{1/3} \left(\frac{k_{\rm B} T_4}{\mu_i m_{\rm H} P_{\rm hot}} \right)^{1/3} \ . \qquad (25)$$

By comparing the number of EUV photons reaching the clump surface per unit time with the recombination rate within the whole clump, one obtains the central clump shielding mass

$$M_{c,sh} = \frac{9}{16} \pi \mu_i m_{\rm H} \alpha_{\rm B}^{-3} \left(\frac{k_{\rm B} T_4}{P_{\rm hot}} \right)^5 q_{UV}^3 R_{SC}^3 . \qquad (26)$$

The first 3.5 Myr of evolution of $M_{\rm c}$ and $M_{\rm c,sh}$ for models A, B and C are shown in Fig 2. Note that for model A which has $\chi > 1$ from the very beginning, the central clump becomes self-shielding at about 1 Myr. For models B and C, the central clump becomes self-shielding as soon as χ becomes larger than 1 at 1.8 and 2.8 Myr, respectively. This is in a relatively good agreement with the numerical simulations of these models (see §5.2), even though self-shielding in model A occurs earlier in the simulation.

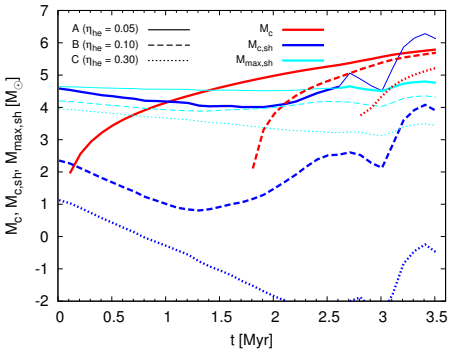

Figure 2. Evolution of the mass of the central clump, $M_{\rm c}$ (red curves), and the corresponding shielding mass, which is the smaller (marked thick) from either $M_{\rm c,sh}$ (blue curves) or $M_{\rm max,sh}$ (cyan curves). The line types denote models A (solid), B (dashed) and C (dotted) with parameters given in Table 1. The clump includes a shielded cold core if $M_{\rm c} > \min(M_{\rm c,sh}, M_{\rm max,sh})$, i.e. if the red curve is above the blue/cyan curve of the same line type.

5.1.2. *Self-shielding of streams*

Since the number of streams of warm gas infalling into the cluster center from different directions cannot be easily determined, we assume that there is only one stream into which all gas inserted below the escape radius $R_{\rm esc}$ accumulates. This implies that the calculated stream shielding mass, $M_{\rm s,sh}$, is a lower limit, as more gas is needed for self-shielding a larger number of streams.

The amount of gas in the stream, $M_{\rm s}$ can be derived by assuming that the time taken for the gas to falls into

[2] Formally, it could happen e.g. in the case when the size of the central clump exceeds $R_{\rm SC}$ since the number of EUV photons entering the clump scales with the clump surface.

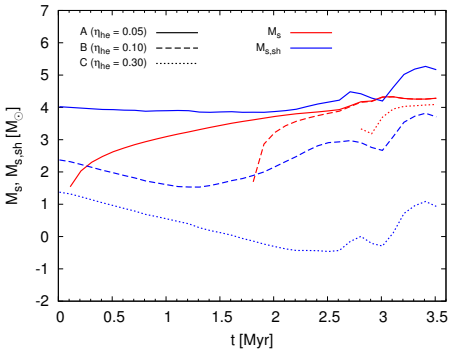

Figure 3. Evolution of the mass of the stream, $M_{\rm s}$ (red curves), and the corresponding shielding mass, $M_{\rm s,sh}$ (blue curves) for models A (solid), B (dashed) and C (dotted) with parameters given by Table 1. The stream includes shielded cold interior if $M_{\rm s} > \min(M_{\rm s,sh}, M_{\rm max,sh})$, i.e. if the red curve is above the blue curve of the same line type. Note that for the shown models, it is always $M_{\rm s,sh} < M_{\rm max,sh}$, and therefore $M_{\rm max,sh}$ is not plotted.

the cluster center is similar to the free fall time $t_{\rm ff}(R_{\rm esc})$ given by Equation 5. The mass of the stream is

$$M_{\rm s}(t) = \int_{t-t_{\rm ff}}^{t} \int_{0}^{R_{\rm esc}} [q_m(r,t') - q_{m,crit}(r,t')] dr dt', \quad (27)$$

which applies for $t - t_{\rm ff} > t_{bs}$ when the hot medium inside the cluster is thermally unstable.

The ionizing EUV photons from the cluster invade the stream upon reaching its surface, which is $\pi d R_{\rm esc}$, where d is the stream diameter. The number of photons arriving per unit time and per unit area was estimated by Palouš et al. (2014) as $\frac{1}{4} q_{UV} R_{SC}$, where q_{UV} is the total EUV photon production rate density of the cluster. At the self-shielding time $t_{\rm s,sh}$, the number of recombinations inside the stream is just in balance with the total number of incoming ionizing photons

$$\pi \frac{d^2}{4} R_{\rm esc} n_4^2 \alpha_{\rm B} = \pi d R_{\rm esc} \frac{1}{4} q_{\rm UV} R_{\rm SC}, \quad (28)$$

where n_4 is the particle density in the stream computed from the pressure balance between the stream and the surrounding hot gas $n_4 = \frac{P_{\rm hot}}{k_{\rm B} T_4}$. The stream shielding mass is

$$M_{\rm s,sh}(t) = \frac{\pi}{4} d^2 R_{esc} \rho \quad (29)$$

with the density $\rho = \mu_{\rm i} m_{\rm H} n_4$. Inserting d from Equation (28) into Equation (29) we get

$$M_{\rm s,sh}(t) = \frac{\pi}{4} q_{\rm UV}^2 R_{\rm SC}^2 R_{\rm esc} \alpha_{\rm B}^{-2} \mu_i m_{\rm H} \left(\frac{k_{\rm B} T_4}{P_{\rm hot}} \right)^3. \quad (30)$$

The evolution of the $M_{\rm s}(t)$ during the first 3.5 Myr of the cluster evolution is compared to the $M_{\rm s,sh}$ evolution in Figure 3, where models A, B and C are shown. For model A, $M_{\rm s}$ is always smaller than $M_{\rm s,sh}$ (apart from a very short interval with $M_{\rm s} \lesssim M_{\rm s,sh}$ at 3 Myr), and thus the stream is not able to self-shield, and remains fully ionized throughout the evolution. For models B and C, the stream mass $M_{\rm s}$ is always larger than $M_{\rm s,sh}$, and thus the streams are able to self-shield their interiors immediately after the start of thermal instabilities. This is in good agreement with the numerical simulation in §5.2.

5.2. *Radiation-hydrodynamic simulations*

The behavior of models is governed mainly by the ratio $\chi \equiv L_{\rm SC}/L_{\rm crit}$. If it is smaller than 1, the stationary solution exists and simulations exhibit a spherically symmetric quasi-stationary distribution of the wind quantities, in a nearly perfect agreement with the semi-analytic code. The wind reaches the sound speed at $r = R_{\rm SC}$ and at a certain radius, $R_{\rm cool} > R_{\rm SC}$, the wind cools down to temperatures $\sim 10^4$ K. The radius $R_{\rm cool}$ decreases with increasing χ, approaching $R_{\rm SC}$ from the outside.

In models for which χ exceeds 1, at time defined as $t_{\rm bs}$ (see Table 2 for $t_{\rm bs}$ for individual models), clumps start to form rapidly inside the cluster. All models exhibit one of the two qualitatively different behaviors illustrated by Figure 4 for model A. The four panels in each row display (from left to right) the particle density in the plane intersecting the cluster center, the temperature in the same plane, the column density of gas and the radial velocity in the central plane. The top row is for time 0.1 Myr when χ just exceeds 1 and the simulation shows individual clumps that are either falling into the center, or leaving the cluster at its periphery. The bottom row, made at 1 Myr when $\chi \approx 2$, shows continuous streams of warm gas that are flowing into the central region. There, the central clump includes the cold core in which sink particles are formed.

Figure 5 compares the behavior of models A, B and C at 3.075 Myr when $\chi > 1$ for all models and they have all accumulated a substantial amount of gas. On the temperature plots (top row) we see that the low heating efficiency (model A) leads to a lower temperature of the hot gas and to a smaller radius at which the wind cools from hot to warm. Further we see that the cold gas (i.e. shielded regions) exists only in the center in model A. In model B, vast majority of the cold gas is located also in the cluster center, however, self-shielding occurs scarcely also at higher radii. In model C, small clumps throughout the whole cluster become ordinarily self-shielding and cold in their interiors. This is in a good agreement with the prediction of the semi-analytic model (cf. to Figures 2 and 3). The middle row of Figure 5 (gas column density) shows that the low heating efficiency (model A) results in a higher volume filling factor of warm gas oc-

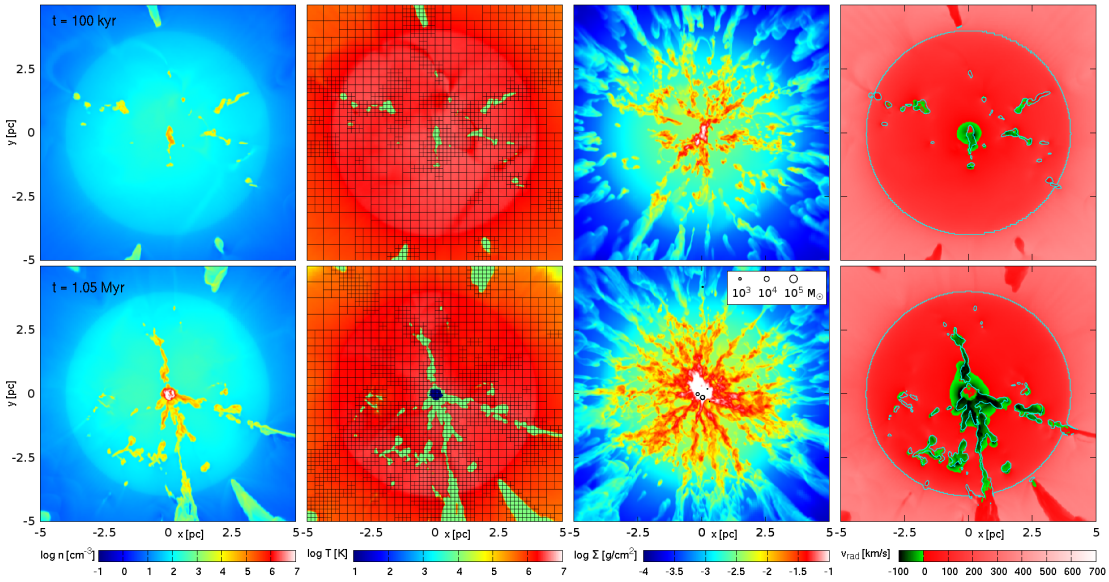

Figure 4. RHD simulation of model A shown for times 100 kyr (top row of panels) and 1.05 Myr (bottom row). Individual columns of panels show (from left to right): (i) logarithm of the gas particle density in plane $z = 0$, (ii) logarithm of the gas temperature in the same plane, grid of black lines shows Flash AMR blocks, (iii) gas column density integrated along the z-direction, and (iv) the gas radial velocity relative to the cluster center, green-black corresponds to inwards velocity, red-white is the outwards velocity, the cyan line separates regions with subsonic and supersonic velocity. The bottom panel (iii) with the gas column density shows also sink particles represented by white circles with black borders, and sizes representing their masses as given in the legend.

Table 2. Properties of studied models.

Model	$t_{\rm bs}$ (Myr)	$t_{\rm c,sh}$ (Myr)	$t_{\rm s,sh}$ (Myr)	$M_{\rm tot}$ (10^5 M$_\odot$)	$M_{\rm acc}$ (10^5 M$_\odot$)	$M_{\rm acc}^{\rm num}$ (10^5 M$_\odot$)	$M_{\rm acc,gas}^{\rm num}$ (10^5 M$_\odot$)
(1)	(2)	(3)	(4)	(5)	(6)	(7)	(8)
A	–	1.0	–	6.9	6.2	6.1	0.14
B	1.8	1.8	1.8	6.9	4.8	4.7	0.18
C	2.8	2.8	2.8	6.9	1.3	1.2	0.24

NOTE— Columns: (1) Model name. (2) Time of the beginning of the thermal instability, $t_{\rm bs}$. (3) Beginning of the central clumps self-shielding, $t_{\rm c,sh}$. (4) Beginning of the infalling stream self-shielding, $t_{\rm s,sh}$. (5) Total amount of reinserted gas including mass loading. (6) Amount of the accumulated gas (semi-analytic model). (7) Amount of the accumulated gas (numerical model). (8) Amount of the remaining warm gas in the computational domain at the end of the evolution (numerical model).

curring in radially inflowing streams, while the higher heating efficiency model C leads to a lower volume filling factor of warm gas in chaotically distributed dense clumps. The radial velocity maps (bottom row of Figure 5) show the dense gas concentrated in streams (in models A and B) flowing inwards from almost all the cluster volume. On the other hand, clumps in model C have inward velocities at small radii and outward velocities at larger radii. This is in agreement with the semi-analytic model that assumes that clumps formed below $R_{\rm esc}$ fall to the center while those forming above $R_{\rm esc}$ flow out of the cluster. The escape radii are, at a given time, $R_{\rm esc}$ = 5.2, 4.0 and 2.4 pc, for models A, B and C, respectively.

The distribution of sink particles, shown together with the column density in the middle row panels of Figure 5, follows closely the distribution of the cold gas. In models A and B with the cold gas only in the center, a single very massive ($\sim 10^5$ M$_\odot$) particle is formed accreting onto itself all cold gas[3]. On the other hand, in model C, several tens of sink particles are formed with masses $10^2 - 10^3$ M$_\odot$ distributed throughout the cluster volume. As stated before, the simulations are unable to resolve individual stellar masses and therefore sink particles represent clusters of stars or stellar associations rather than individual objects. Due to the extremely simplified physics of star formation, sink particles are here regarded as trac-

[3] Initially, several sinks are formed in model A, however, all except one are ejected by dynamical interactions with the most massive sink and infalling gaseous clumps.

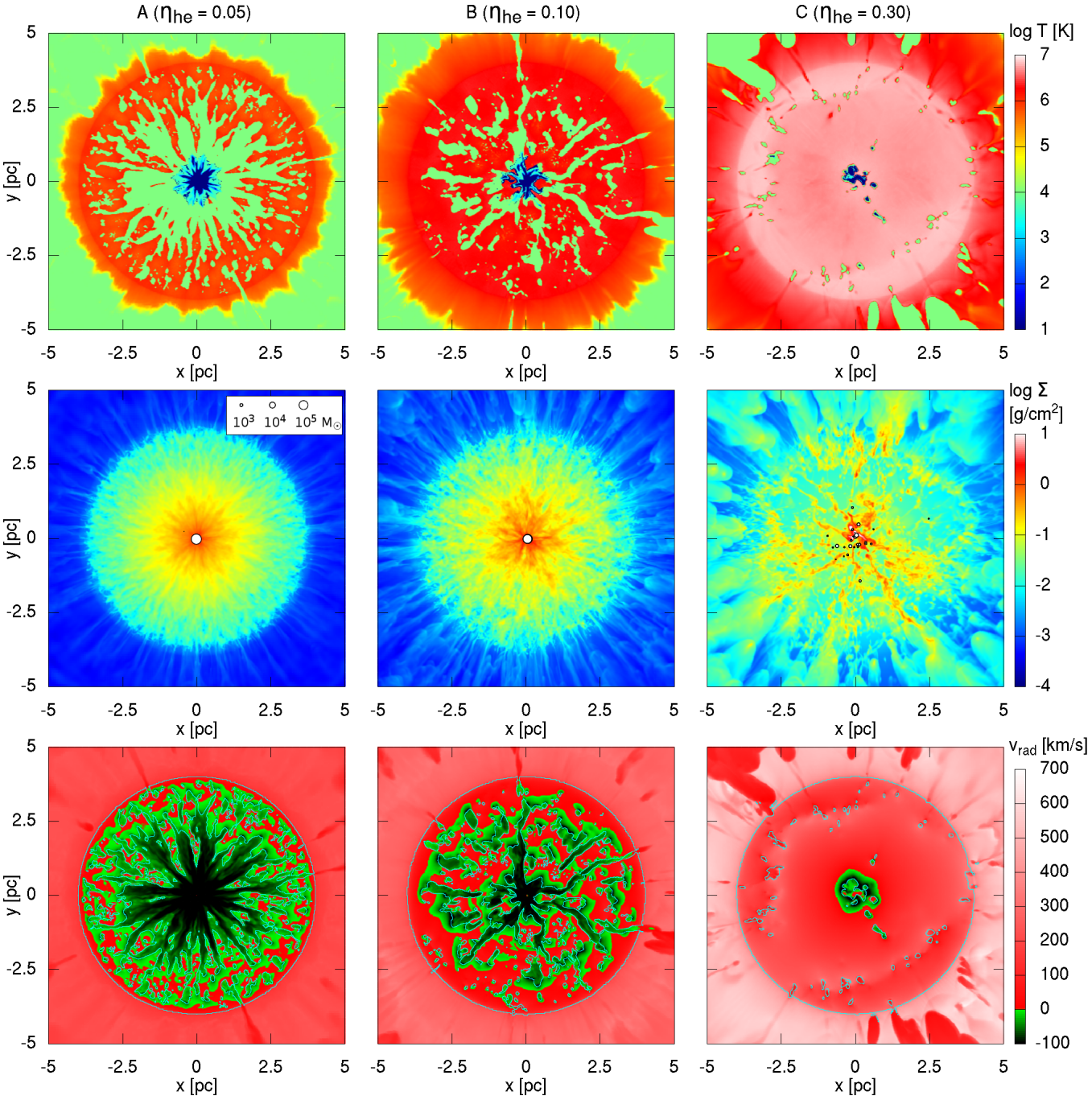

Figure 5. Comparison of RHD simulations of models A, B and C (columns from left to right) at time 3.075 Myr. The top row shows the logarithm of the gas temperature in plane $z = 0$; the middle row is the column density integrated along the z-direction; and the bottom row presents the gas radial velocity relative to the cluster center, green-black corresponds to inwards velocity, red-white is the outwards velocity, the cyan line separates regions with subsonic and supersonic velocity. Sink particles are shown in the middle row by white circles with black borders, and sizes representing their masses as given in the legend.

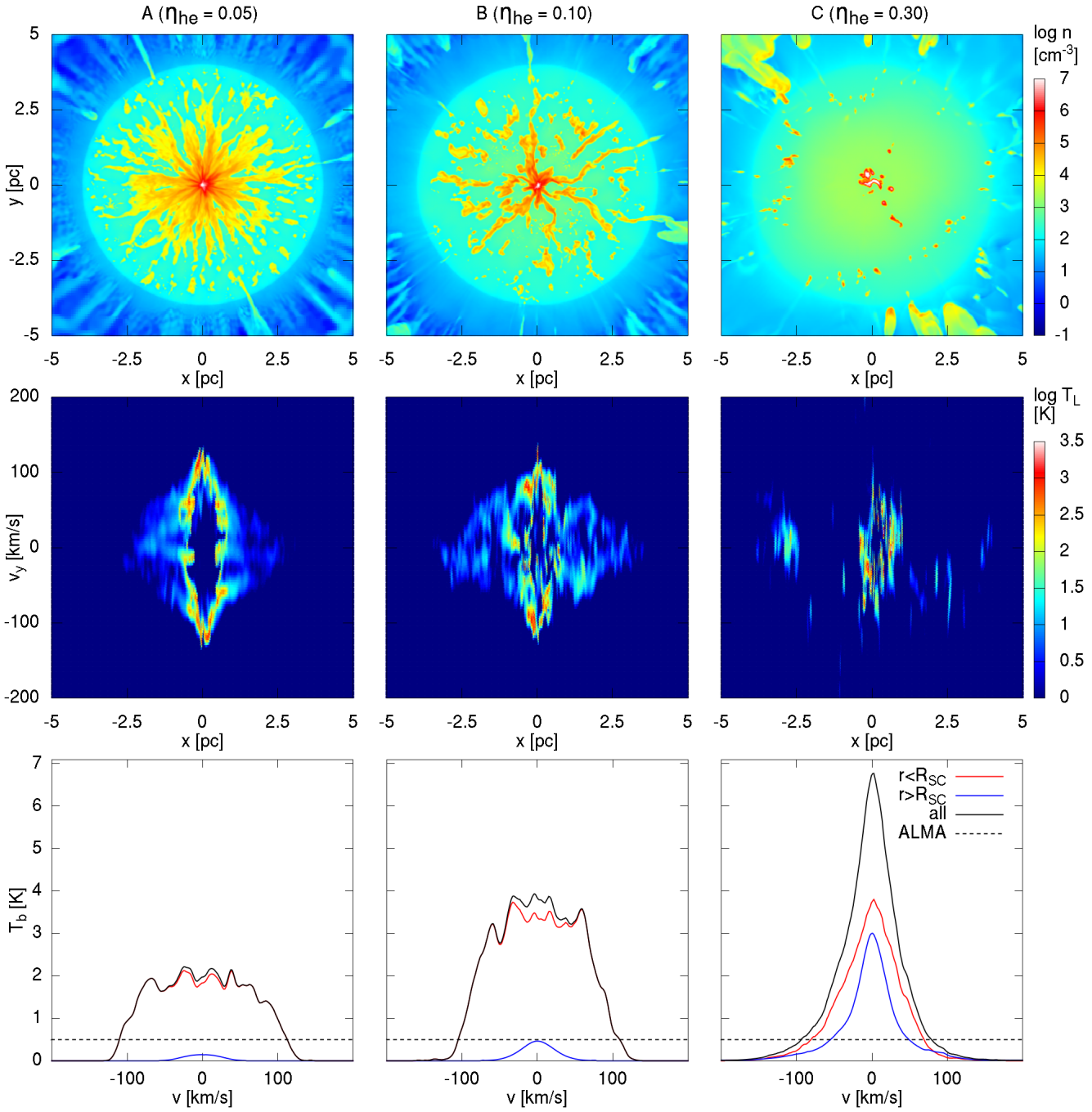

Figure 6. Comparison of emission line synthetic observations for models A, B and C (columns from left to right) at time 3.075 Myr. The top row shows the logarithm of the gas particle density in plane $z = 0$; the middle row shows the position-velocity ($x - v_y$) diagram of the synthetic recombination line emission from the $z = 0$ plane only; and the bottom row presents synthetic line emission integrated over the whole computational domain. The line profile is calculated as seen from the x-direction and the total emission (black) is split into a part coming from within the cluster (red) and from outside of it (blue). The horizontal dashed line ($T_\mathrm{b} = 0.5\,\mathrm{K}$) shows a rough estimate of the ALMA sensitivity with configuration described at the end of §5.2.

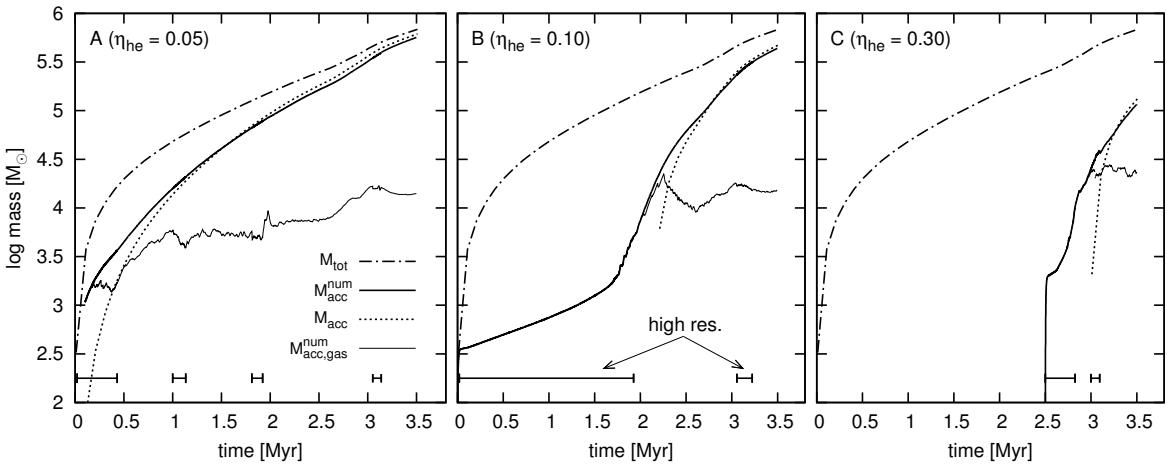

Figure 7. Evolution of the inserted and accumulated mass for models A, B and C (panels left to right). The thick dash-dotted line shows the total amount of gas, $M_{\rm tot}$, inserted to the cluster up to a given time (both winds and mass loading). The thick solid black line denotes mass accumulated in RHD simulation, $M_{\rm acc}^{\rm num}$ (both gas and sink particles), and the thick dotted is the corresponding accumulated mass, $M_{\rm acc}$, estimated by the semi-analytic model. The thin solid line shows the mass, $M_{\rm acc,gas}^{\rm num}$, of the warm and cold gas present in the simulation computational domain, *i.e.* the accumulated mass without sinks. The horizontal lines with T-shaped heads at the bottom of the figures denote periods during which the simulations were calculated at higher resolution (AMR, up to refinement level 7 corresponding to 512^3 maximum resolution).

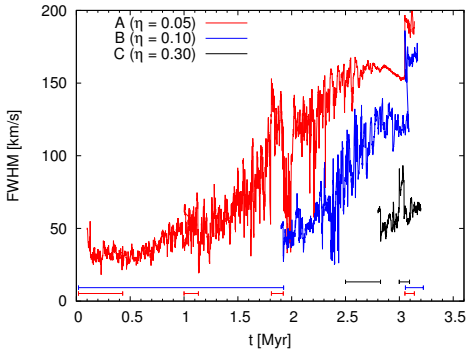

Figure 8. Evolution of the synthetic line widths (FWHM) for models A (red), B (blue) and C (black). The horizontal lines with T-shaped heads and a corresponding color at the bottom denote periods during which the simulations were calculated at higher resolution

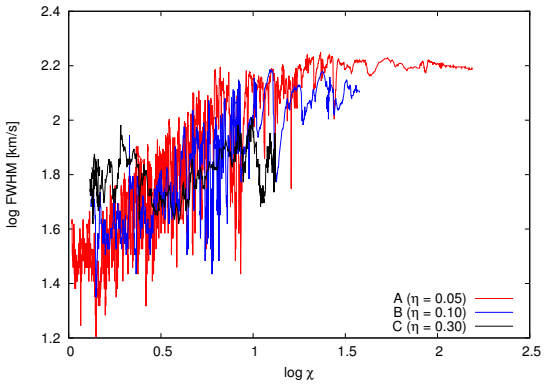

Figure 9. The synthetic line widths (FWHM) for models A (red), B (blue) and C (black) as a function of χ.

ers of the star formation location and their total mass as an upper limit to the mass of second generation stars.

Figure 7 shows the total amount of mass accumulated inside the clusters, $M_{\rm acc}^{\rm num}$ (thick solid line), according to the RHD simulations, as a function of time for models A, B and C. For almost all the time, except a short period after the first sink formation, the accumulated mass is dominated by the mass of sink particles as seen by comparing with the accumulated gas only, $M_{\rm acc,gas}^{\rm num}$ (thin solid line). Further, $M_{\rm acc}^{\rm num}$ is compared to the total amount of mass inserted into the cluster by stellar winds, $M_{\rm tot}(t) = \int_0^t (1+q_m)\dot{M}_{\rm SC}(t')dt'$ (dash-dotted line), and to the semi-analytic estimate of the accumulated mass, $M_{\rm acc}$ (dotted line, Equation 14), derived from semi-analytic calculations. The above quantities at the end of simulations are also given by Table 2. We can see that $M_{\rm acc}^{\rm num}$ is a strong function of $\eta_{\rm he}$: in model A, the majority of the inserted mass stays in the cluster, while in model C, the fraction of accumulated mass is less than 20%. We can also see (both from Table 2 and Figure 7) that the semi-analytic estimates of the accumulated gas are very close to the values obtained from the simulations.

5.3. *Observational predictions*

Synthetic spectra calculated for models A, B and C at time 3.075 Myr are presented in Figure 6. The figure shows the particle density in the $z = 0$ plane (top row), the H30α line emission coming from the same plane in the position-velocity diagram (middle row; Equation 22) and the brightness temperature velocity profile T_b integrated over all grid cells calculated for a virtual telescope with angular resolution $D_{\rm res} = 10\,{\rm pc}$. Note that the line profiles of the three simulated models are considerably different. Model A exhibits a broad (FWHM $\sim 200\,{\rm km\,s^{-1}}$) line with flat and nodulated top. A comparison with the particle density map and the position-velocity diagram shows that the majority of the emission comes from the central region with many dense warm inflowing streams. The highest velocity of the emitting gas occurs close to the center where the streams are accelerated to velocity $\sim 100\,{\rm km\,s^{-1}}$ by the gravitational field of the cluster and the central sink particle. In the very center, the infalling gas becomes shielded and cold and stops to emit in the recombination line. In this way, the radius at which self-shielding occurs determines the FWHM of the line. On the other hand, the line profile of model C is much narrower (FWHM $\sim 100\,{\rm km\,s^{-1}}$) and it has a sharp peak. Here the emission arises from contributions of many small dense warm clumps with both inwards and outwards velocities (see the bottom panel of Figure 5). The line profile of model B is a transition between the other two cases, although it seems qualitatively closer to model A. A decomposition of T_b into emission coming from $r < R_{\rm SC}$ and from $r > R_{\rm SC}$ (red and blue curves, respectively) shows that the majority of emission comes from within the cluster in models A and B and that the emission from both regions is comparable in model C.

Figure 8 shows the evolution of the FWHM of the synthetic H30α lines for the three calculated models. One can appreciate two general trends: (i) the line width grows with time for all models, and (ii) the line width decreases with increasing $\eta_{\rm he}$. All FWHM curves also exhibit sudden growths at times when the resolution increases and sudden drops at times when the resolution decreases. This can be understood as a consequence of the cold regions not being properly resolved: the majority of high velocity emission comes from the dense warm gas flowing into the cold regions. The higher resolution leads to smaller cold regions with the inflowing warm gas reaching higher densities and velocities. This implies that the line profiles and widths, regardless of the amount of accumulated mass, are not well resolved with the numerical resolution used and therefore should be taken just as indicators of general trends and not to draw quantitative predictions.

Figure 9 shows the FWHM of the synthetic lines as a function of χ. Models A and B show a very similar behavior: the FWHM grows with χ monotonically for $\log(\chi)$ between 0 and ~ 1.2 and stays approximately constant for higher values. Since in both models the dense warm gas occurs mainly in the inflowing streams, we interpret it so that the FWHM is given by the maximum velocity of streams. Greater value of χ leads to higher $R_{\rm esc}$, and therefore streams inflow into the center from larger radii and with higher velocity leading to the growth of FWHM with χ. For $\log(\chi) \gtrsim 1.2$ the outer boundaries of the streams reach almost the cluster border, and therefore their growth is not further possible and FWHM(χ) saturates. On the other hand, model C does not show a clear FWHM(χ) dependence. This most likely is because the emission in this model comes mainly from individual clumps formed at various radii having more random (both inwards and outwards) velocities.

Finally, we estimate the observability of the warm gas predicted by the simulations. The closest known objects with comparable parameters (mass, radius, age) are super star clusters in the interacting galaxies NGC4038/9 (Antennae). At their approximate distance $\sim 20\,{\rm Mpc}$ (Schweizer et al. 2008) and diameters $\sim 10\,{\rm pc}$, the correponding angular resolution is $D_{\rm res} \sim 0.1$". Using the ALMA sensitivity calculator, we estimate the integration time needed to reach sensitivity 0.5 K (shown as dashed horizontal lines in the bottom panels of Figure 6) with 40 12m antennae and bandwidth $200\,{\rm km\,s^{-1}}$ to be 18 mins. Therefore, we conclude that it should be in principle possible to test the presented model with observations using the appropriate ALMA configurations.

5.4. *Parameter space study*

Motivated by the excellent agreement between the accumulated mass in numerical models $M_{\rm acc}^{\rm num}$ and the semi-analytic estimate $M_{\rm acc}$ we consider a larger subset of the parameter space $\eta_{\rm he}$-$\eta_{\rm ml}$ using the semi-analytic code. We calculate a grid of models with parameters given in Table 1 (which correspond to our numerical models A, B and C) and vary the heating efficiency and the mass loading in intervals $\eta_{\rm he} \in (0.001, 1)$ and $\eta_{\rm ml} \in (0, 5)$. For each model we calculate the first 3.5 Myr of the evolution and evaluate: (i) whether rapid cooling occurs during that period (i.e. $\chi > 1$), (ii) whether the central clump becomes self-shielding (i.e. $M_{\rm c} \equiv M_{\rm acc} > \min(M_{\rm max,sh}, M_{\rm c,sh})$, see Equations 14, 26 and 24), (iii) whether the infalling stream becomes self-shielding (i.e. $M_{\rm s} > \min(M_{\rm max,sh}, M_{\rm s,sh})$, see Equations 14, 27 and 30), and (iv) if self-shielding occurs, what is the amount of accumulated gas $M_{\rm acc}$ (Equation 14).

The resulting map of the $\eta_{\rm he}$-$\eta_{\rm ml}$ parameter space is shown in Figure 10. The color represents the amount of accumulated gas, $M_{\rm acc}$, and it is plotted only if self-shielding occurs (otherwise, it is left white). We can

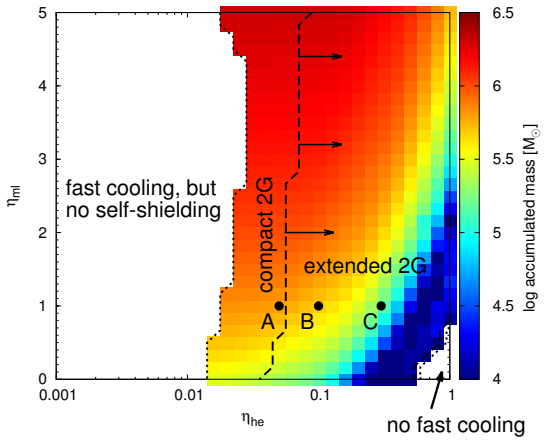

Figure 10. Map of the $\eta_{\rm he}$-$\eta_{\rm ml}$ parameter space for models with parameters given by Table 1. The color shows the amount of mass accumulated during first 3.5 Myr for a model with given parameters. The dotted and dashed lines separate four qualitatively different regions described in the text (see §5.4). Location of models A, B and C is shown by black circles. Horizontal arrows attached to the dashed vertical line denote that it should be interpreted as a lower limit.

identify four qualitatively different regions. First, a small region with high $\eta_{\rm he}$ and small $\eta_{\rm ml}$ (bottom right) where χ never exceed 1 and rapid cooling does not occur. Second, the region with $\eta_{\rm he} \lesssim 0.02$ where even though rapid cooling occurs inside the cluster, the gas never achieves self-shielding. This is because low $\eta_{\rm he}$ leads to relatively low pressure and hence to a low warm gas density, and therefore all the warm gas that can be accommodated inside the cluster is ionized by the EUV radiation from the stars. Consequently, in these two regions secondary star formation is inhibited. The third region lies between $\eta_{\rm he} \sim 0.02$ and $0.05 - 0.08$ (marked "compact 2G", includes model A); here rapid cooling occurs and the central clump is able to self-shield. However, due to the relatively low density of the warm gas, the infalling streams are never dense and massive enough to reach self-shielding. In this case, secondary star formation becomes possible only in the central clump. In the fourth region with $0.05-0.08 < \eta_{\rm he} < 0.8-1$ (marked extended 2G, includes models B and C), both the central clump and the infalling streams achieve self-shielding conditions and thus secondary star formation becomes possible in both the central clump and the infalling streams. The vertical dashed line separating the third and the fourth region represents only a lower limit on $\eta_{\rm HE}$ and the more realistic border between those two regions lies probably slightly rightwards (see below). This is indicated by horizontal arrows attached to the vertical dashed line.

Numerical models A, B and C are denoted by black circles in Figure 10. Model A lies in the region predicting a compact and central 2G sub-cluster formation, in good agreement with the numerical results. Throughout the whole evolution, only the central clump is self-shielding, and sink particles form only in the very center. Similarly, model C lies in the region where the extended 2G sub-cluster should be formed, and again it is in a good agreement with the model behavior. The gas becomes self-shielding even at larger radii while falling into the cluster center, and a larger number of less massive sink particles form throughout the cluster. On the other hand, model B lies also in the region of "extended 2G", but its behavior is closer to that of model A. This implies that the line separating "compact 2G" and "extended 2G" regions marks only a lower limit in $\eta_{\rm he}$. The model is classified as the one with an "extended 2G" if during the calculation there is a period when $M_{\rm s} > M_{\rm s,sh}$. As this period can be arbitrarily short, the majority of stars can still form in the central clump. Moreover, the criterion only evaluates whether self-shielding in streams occur, but the semi-analytic model is unable to calculate whether the cold gas collapses into stars / sink particles. The top middle panel of Figure 5 indeed shows that self-shielding can rarely and marginally occur also at large radii. Therefore we conclude that the more realistic estimate of the location of the line separating "compact 2G" and "extended 2G" would be somewhere between the calculated line and the position of model C, i.e. approximately at $\eta_{\rm he} = 0.08 - 0.3$.

6. DISCUSSION

The model used in this work includes many simplifications and caveats. Here we list the ones that we consider most important. One of the most serious problems is probably the unknown origin of the low heating efficiency treated as a free parameter. In principle, it can be any type of additional cooling, not accounted for by the gas cooling included in our model. One possibility could be cooling at the transition layer between the hot gas and warm clumps combined with the thermal conduction transporting the heat from the hot gas onto clump surfaces. We plan to explore this option in future work. Inclusion of the thermal conduction leading to evaporation of pre-existing clumps may also provide self-consistent mechanism for mass loading, which is here also treated as a free parameter. Furthermore, the physics of gas with temperatures below 10^4 K and 2G star formation process is extremely simplified in the numerical code and not present in the semi-analytic model. As a result, the 2G mass is probably overestimated and the provided values should be contemplated rather as upper limits. Feedback from the 2G stars is also missing, even though it probably behaves in a similar way as feedback from 1G stars, and can be considered as a local enhancement of

mass and energy deposition rates within the framework of the model. Another simplification is the distribution of wind mass and energy, in our model evenly supplied within the cluster volume, assuming that the wind-wind collisions redistribute smoothly the mass and mechanical energy of the winds. This has been well justified by Cantó et al. (2000, 2006) for adiabatic models, however, the applicability of this approach in case of more complex physics including cooling and radiation is less clear.

The presented model predicts the formation of 2G stars out of stellar winds from the 1G. Such models have already been suggested e.g. by Decressin et al. (2007b) and D'Ercole et al. (2010). However, our model exhibits two unique features. Firstly, it predicts that even fast stellar winds with velocities exceeding thousands of km/s can be captured inside the cluster and 2G stars can form out of them, while all previous models assumed that stellar winds have to be slow (e.g. D'Ercole et al. 2008) in order to contribute to 2G star formation. Moreover, the model makes a clear link between the cluster global properties and the secondary star formation by predicting that it can occur only if the cluster is massive and compact enough (i.e. $L_{\rm SC} > L_{\rm crit}$). Another unique feature is that our model provides a self-consistent mechanism predicting that 2G stars form in a small central part of the cluster if the heating efficiency is small. The existing models (see e.g. Krause et al. 2013) sometimes assume that 2G stars can form in the cluster central region, because they form out of massive stars located close to the center due to primordial mass segregation. However, it is only an assumption and the hypothesis of primordial mass segregation has been questioned by recent observations of NGC3603 with VLT/SPHERE using extreme adaptive optics (Khorrami et al. 2016).

The model predicts secondary star formation occurring in young massive clusters with solar metallicity, and it therefore naturally raises the question of whether it could be tested by observations of nearby young massive clusters. Photometric observations of intermediate age (Bertelli et al. 2003; Mackey et al. 2008; Milone et al. 2009) and recently even young (Milone et al. 2015, 2016) massive clusters in the LMC indeed suggest the presence of multiple stellar populations. However, other explanations of multiple episodes of star formation have been also suggested and recently Milone et al. (2016); Bastian et al. (2016) argue that the effect of stellar rotation may provide the most plausible one. More promising can be the detection of warm dense gas with a high velocity dispersion as suggested in this work. The emission lines showing the presence of the warm gas have been observed in embedded clusters in galaxies as NGC 5253 (Beck et al. 2012; Turner et al. 2015; Smith et al. 2016), NGC 4449 (Sokal et al. 2015) and in Antennae interacting galaxies (Gilbert & Graham 2007). The predicted emission line profiles seems to show a significant differences between the emission of HII regions and the emission from the cluster interior. A more detailed comparison of the predicted versus observed profiles should be performed in the future.

An interesting question is whether the rapidly cooling winds model could explain the origin of multiple stellar populations observed commonly in globular clusters. Formation of globular clusters is a complex field and even though many mechanisms have been suggested, a fully satisfactory model does not seem to exist (Bastian 2015). We have here described a basic mechanism that always leads to rapid cooling and mass accumulation providing there is enough hot and relatively dense gas inside the cluster. Therefore, a critical question determining whether the model could work depends on whether stellar evolution models for low metallicity massive stars predict winds with a large enough mass loss. One possibility could be models of fast rotating massive stars (Decressin et al. 2007b) or massive binaries (de Mink et al. 2009; Tenorio-Tagle et al. 2016). The presented model differs from the other mentioned models by the fact that the wind always goes through the hot phase and contributions from various types of stars and the pristine (mass loaded) gas mix completely together. This, on the one hand, could explain the presence of Li (signature of pristine gas) in 2G stars, on the other hand, it does not seem straight forward to explain the extreme abundance patterns (e.g. the high oxygen depletion), as it only happens in some (very massive) types of stars. A feature in favor of the rapidly cooling winds model is the mentioned self-consistent mechanism predicting the formation of 2G stars in the very center, which provides an ideal setup for the removal of 1G stars by combination of gas expulsion and tidal forces as described in Khalaj & Baumgardt (2015). Another attractive feature of our model is the link between secondary star formation and the global parameters of the cluster (mass, radius, metallicity, ...), which provides a natural explanation as to why only globular clusters (or in general massive cluster), and not less massive open cluster or field stars, exhibit features related to multiple stellar populations.

7. CONCLUSIONS

We have studied a model of *rapidly cooling shocked stellar winds* in young massive clusters and estimate the circumstances under which secondary star formation, out of the reinserted winds from a first stellar generation is possible. We have used two implementations of the model: a highly idealized computationally inexpensive spherically symmetric semi-analytic model, and a complex three-dimensional radiation-hydrodynamic simulations. The model determines whether the hot shocked stellar winds inside the cluster become thermally unsta-

ble and form dense clumps, whether these clumps self-shield against the stellar EUV radiation and cool further where ever it may happen. The model also determines the fraction of stellar wind mass that cools down and feeds secondary star formation. Both implementations show a good agreement for the three calculations made with different values of the heating efficiency of the shocked stellar winds. Further, we have used the semi-analytic model to explore a subset of the parameter space covering a wide range of the observationally poorly constrained parameters: the heating efficiency, $\eta_{\rm he}$, and the mass loading, $\eta_{\rm ml}$. Finally, we have calculated the emission in the H30α recombination line, analyzed its velocity profile and estimated its intensity for super star clusters at the distance of the interacting galaxies NGC4038/9 (Antennae).

Our conclusions are as follows:

1. With more accurate and complex numerical model including gravity and ionizing radiation we confirm our previous findings (Tenorio-Tagle et al. 2005a; Wünsch et al. 2008) that in young, massive and compact clusters, the resultant thermalized shocked stellar winds become thermally unstable. This leads to the formation of dense warm clumps before leaving the cluster volume while composing a cluster wind. The dense clumps cool further as they self-shield themselves from the EUV radiation, triggering then the formation of next generations of stars. In this way, the reinserted stellar wind material, expected in adiabatic calculations to be expelled from the cluster volume with velocities largely exceeding the escape velocity of the cluster, can be captured and used for secondary star formation.

2. The fraction of the mass reinserted through 1G stellar winds which accumulates inside the cluster and becomes available for secondary star formation is a function of cluster parameters, and it can be large ($> 50\%$) for sets of reasonable parameter. Specifically, for clusters with 1G stellar mass $\sim 10^7\,{\rm M}_\odot$, half-mass radius 2.38 pc, mass loading $\eta_{\rm ml} = 1$ and heating efficiencies 0.05, 0.1 and 0.3, the fractions are 88 %, 68 % and 17 %, respectively. The corresponding masses of gas available for secondary star formation are 6.1×10^5, 4.7×10^5 and $1.2 \times 10^5\,{\rm M}_\odot$. Thus our model suffers also the "mass budget problem" encountered in former scenarios trying to explain multiple populations observed in globular clusters: the mass fraction of the second stellar generation is too low unless a substantial fraction of 1G stars are later removed from the cluster.

3. The presented model provides a self-consistent mechanism predicting the formation of 2G stars only in the central zones of the cluster. The crucial parameter determining where the 2G stars form is the heating efficiency: if it is low (of order $1-10\%$), 2G stars form only in the center; if it is larger, 2G stars form everywhere throughout the cluster (see regions "compact 2G" and "extended 2G" on the parameter space map in Figure 10). The heating efficiency is closely related to the temperature of the hot shocked wind within the cluster and there is some observational evidence, that it may indeed be low (Silich et al. 2009; Rosen et al. 2014). This is interesting in terms of the aforementioned mass budget problem, because if 1G and 2G stars are spatially separated in this way, a substantial fraction of 1G stars can be lost due to the primordial gas expulsion and the subsequent dynamical evolution (Khalaj & Baumgardt 2016).

4. The model predicts that a cluster with studied parameters and age $2-3$ Myr should contain in its interior a dense warm gas in amounts of the order of $10^4\,{\rm M}_\odot$. This gas can be traced e.g. by observing hydrogen recombination lines. The line widths predicted by the model are in an approximate agreement with observations of Brγ line for super star clusters in Antennae galaxies (Gilbert & Graham 2007). The intensities of the H30α radio recombination line calculated for the modelled cluster at the distance of Antennae should make the warm gas detectable with the convenient configuration of ALMA at reasonable integration times.

We thank the anonymous referee for constructive and valuable comments. We thank Dorottya Szécsi for careful reading of the text and her useful suggestions. This study has been supported by project 15-06012S of the Czech Science Foundation, the institutional project RVO:67985815, the CONACYT-México research grant 167169, the Bilateral agreement between CONACYT and the Czech Academy of Sciences grant 17048, and the ISSI project "Massive star clusters across the Hubble time". This work was supported by The Ministry of Education, Youth and Sports from the Large Infrastructures for Research, Experimental Development and Innovations project "IT4Innovations National Supercomputing Center LM2015070".

REFERENCES

Bastian, N. 2015, IAU Symposium 316 "Formation, evolution, and survival of massive star clusters", arXiv:1510.01330

—. 2016, in "EES2015 - Stellar Clusters: benchmarks of stellar physics and galactic evolution", eds. E. Moraux, Y. Lebreton and C. Charbonnel, arXiv:1606.09468
Bastian, N., Niederhofer, F., Kozhurina-Platais, V., et al. 2016, MNRAS, 460, L20
Beck, S. C., Lacy, J. H., Turner, J. L., et al. 2012, ApJ, 755, 59
Bedin, L. R., Piotto, G., Anderson, J., et al. 2004, ApJL, 605, L125
Bertelli, G., Nasi, E., Girardi, L., et al. 2003, AJ, 125, 770
Binney, J., & Tremaine, S. 2008, Galactic Dynamics: Second Edition (Princeton University Press)
Cantó, J., Raga, A. C., & Adame, L. 2006, MNRAS, 369, 860
Cantó, J., Raga, A. C., & Rodríguez, L. F. 2000, ApJ, 536, 896
Carretta, E., Bragaglia, A., Gratton, R., & Lucatello, S. 2009, A&A, 505, 139
Carretta, E., Bragaglia, A., Gratton, R. G., et al. 2006, A&A, 450, 523
Chevalier, R. A., & Clegg, A. W. 1985, Nature, 317, 44
Clark, P. C., Glover, S. C. O., & Klessen, R. S. 2012, MNRAS, 420, 745
Colella, P., & Woodward, P. R. 1984, Journal of Computational Physics, 54, 174
de Mink, S. E., Pols, O. R., Langer, N., & Izzard, R. G. 2009, A&A, 507, L1
Decressin, T., Charbonnel, C., & Meynet, G. 2007a, A&A, 475, 859
Decressin, T., Meynet, G., Charbonnel, C., Prantzos, N., & Ekström, S. 2007b, A&A, 464, 1029
D'Ercole, A., D'Antona, F., Ventura, P., Vesperini, E., & McMillan, S. L. W. 2010, MNRAS, 407, 854
D'Ercole, A., Vesperini, E., D'Antona, F., McMillan, S. L. W., & Recchi, S. 2008, MNRAS, 391, 825
Espinoza, P., Selman, F. J., & Melnick, J. 2009, A&A, 501, 563
Federrath, C., Banerjee, R., Clark, P. C., & Klessen, R. S. 2010, ApJ, 713, 269
Fryxell, B., Olson, K., Ricker, P., et al. 2000, ApJS, 131, 273
Gilbert, A. M., & Graham, J. R. 2007, ApJ, 668, 168
Górski, K. M., Hivon, E., Banday, A. J., et al. 2005, ApJ, 622, 759
Hueyotl-Zahuantitla, F., Palouš, J., Wünsch, R., Tenorio-Tagle, G., & Silich, S. 2013, ApJ, 766, 92
Hueyotl-Zahuantitla, F., Tenorio-Tagle, G., Wünsch, R., Silich, S., & Palouš, J. 2010, ApJ, 716, 324
Khalaj, P., & Baumgardt, H. 2015, MNRAS, 452, 924
—. 2016, MNRAS, 457, 479
Khorrami, Z., Lanz, T., Vakili, F., et al. 2016, A&A, 588, L7
King, I. 1962, AJ, 67, 471
Krause, M., Charbonnel, C., Decressin, T., Meynet, G., & Prantzos, N. 2013, A&A, 552, A121
Krause, M. G. H., Charbonnel, C., Bastian, N., & Diehl, R. 2016, A&A, 587, A53
Kroupa, P. 2001, MNRAS, 322, 231
Leitherer, C., Robert, C., & Drissen, L. 1992, ApJ, 401, 596
Leitherer, C., Schaerer, D., Goldader, J. D., et al. 1999, ApJS, 123, 3
Lohmann, W. 1964, ZAp, 60
Mackey, A. D., Broby Nielsen, P., Ferguson, A. M. N., & Richardson, J. C. 2008, ApJL, 681, L17
MacNeice, P., Olson, K. M., Mobarry, C., de Fainchtein, R., & Packer, C. 2000, Computer Physics Communications, 126, 330
Melo, V. P., Muñoz-Tuñón, C., Maíz-Apellániz, J., & Tenorio-Tagle, G. 2005, ApJ, 619, 270
Mengel, S., Lehnert, M. D., Thatte, N. A., et al. 2008, A&A, 489, 1091
Milone, A. P., Bedin, L. R., Piotto, G., & Anderson, J. 2009, A&A, 497, 755
Milone, A. P., Marino, A. F., D'Antona, F., et al. 2016, MNRAS, 458, 4368
Milone, A. P., Bedin, L. R., Piotto, G., et al. 2015, MNRAS, 450, 3750
Ninkovic, S. 1998, Serbian Astronomical Journal, 158
Osterbrock, D. E. 1974, Astrophysics of gaseous nebulae
Palouš, J., Wünsch, R., Martínez-González, S., et al. 2013, ApJ, 772, 128
Palouš, J., Wünsch, R., & Tenorio-Tagle, G. 2014, ApJ, 792, 105
Piotto, G., Bedin, L. R., Anderson, J., et al. 2007, ApJL, 661, L53
Portegies Zwart, S. F., McMillan, S. L. W., & Gieles, M. 2010, ARA & A, 48, 431
Rohlfs, K., & Wilson, T. L. 2004, Tools of radio astronomy, ed. Rohlfs, K. & Wilson, T. L.
Rosen, A. L., Lopez, L. A., Krumholz, M. R., & Ramirez-Ruiz, E. 2014, MNRAS, 442, 2701
Schure, K. M., Kosenko, D., Kaastra, J. S., Keppens, R., & Vink, J. 2009, A&A, 508, 751
Schweizer, F., Burns, C. R., Madore, B. F., et al. 2008, AJ, 136, 1482
Silich, S., Tenorio-Tagle, G., & Muñoz-Tuñón, C. 2003, ApJ, 590, 791
Silich, S., Tenorio-Tagle, G., Muñoz-Tuñón, C., et al. 2010, ApJ, 711, 25
Silich, S., Tenorio-Tagle, G., & Rodríguez-González, A. 2004, ApJ, 610, 226
Silich, S., Tenorio-Tagle, G., Torres-Campos, A., et al. 2009, ApJ, 700, 931
Smith, L. J., Crowther, P. A., Calzetti, D., & Sidoli, F. 2016, ApJ, 823, 38
Sokal, K. R., Johnson, K. E., Indebetouw, R., & Reines, A. E. 2015, AJ, 149, 115
Strickland, D. K., & Heckman, T. M. 2009, ApJ, 697, 2030
Tenorio-Tagle, G., Muñoz-Tuñón, C., Cassisi, S., & Silich, S. 2016, ApJ, 825, 118
Tenorio-Tagle, G., Silich, S., Martínez-González, S., et al. 2013, ApJ, 778, 159
Tenorio-Tagle, G., Silich, S., Rodríguez-González, A., & Muñoz-Tuñón, C. 2005a, ApJL, 628, L13
—. 2005b, ApJ, 620, 217
Tenorio-Tagle, G., Wünsch, R., Silich, S., Muñoz-Tuñón, C., & Palouš, J. 2010, ApJ, 708, 1621
Tenorio-Tagle, G., Wünsch, R., Silich, S., & Palouš, J. 2007, ApJ, 658, 1196
Turner, J. L., Beck, S. C., Benford, D. J., et al. 2015, Nature, 519, 331
Westmoquette, M. S., Smith, L. J., Gallagher, III, J. S., et al. 2007, ApJ, 671, 358
Whitmore, B. C., & Schweizer, F. 1995, AJ, 109, 960
Wünsch, R., Silich, S., Palouš, J., Tenorio-Tagle, G., & Muñoz-Tuñón, C. 2011, ApJ, 740, 75
Wünsch, R., Tenorio-Tagle, G., Palouš, J., & Silich, S. 2008, ApJ, 683, 683